PNAS RESEARCH ARTICLE | EARTH, ATMOSPHERIC, AND PLANETARY SCIENCES
ASTRONOMY

Coupled atmospheric chemistry, radiation, and dynamics of an exoplanet generate self-sustained oscillations

Yangcheng Luo[a,b,c], Yongyun Hu[b,1], Jun Yang[b], Michael Zhang[a], and Yuk L. Yung[a,1]

Edited by Neta Bahcall, Princeton University, Princeton, NJ; received June 4, 2023; accepted October 13, 2023

Nonlinearity in photochemical systems is known to allow self-sustained oscillations, but they have received little attention in studies of planetary atmospheres. Here, we present a unique, self-oscillatory solution for ozone chemistry of an exoplanet from a numerical simulation using a fully coupled, three-dimensional (3D) atmospheric chemistry-radiation-dynamics model. Forced with nonvarying stellar insolation and emission flux of nitric oxide (NO), atmospheric ozone abundance oscillates by a factor of thirty over a multidecadal timescale. As such self-oscillations can only occur with biological nitrogen fixation contributing to NO emission, we propose that they are a unique class of biosignature. The resulting temporal variability in the atmospheric spectrum is potentially observable. Our results underscore the importance of revisiting the spectra of exoplanets over multidecadal timescales to characterizing the atmospheric chemistry of exoplanets and searching for exoplanet biosignatures. There are also profound implications for comparative planetology and the evolution of the atmospheres of terrestrial planets in the solar system and beyond. Fully coupled, 3D atmospheric chemistry-radiation-dynamics models can reveal new phenomena that may not exist in one-dimensional models, and hence, they are powerful tools for future planetary atmospheric research.

exoplanets | photochemistry | self-oscillations | ozone | nonlinearity

Significance

Using a fully coupled, three-dimensional atmospheric chemistry-radiation-dynamics model, we demonstrate that the atmospheric composition of terrestrial exoplanets can be self-oscillatory under nonvarying external forcings. This finding could inspire future research on nonlinear behaviors in diverse photochemical systems on exoplanets. The simulated temporal variability of the ozone layer is large enough to be detected by future space telescopes. As the photochemical self-oscillations in our simulations can only exist with a strong surface NO_x source, the resulting large, periodic oscillations of ozone abundance, once observed, could suggest the presence of biological nitrogen fixation, hence they are proposed as a unique class of exoplanet biosignature.

In photochemical studies of planetary atmospheres, it is generally assumed that if all external forcings, such as insolation and emission rates, are nonvarying, any initial value problem can ultimately reach a unique steady state. However, it has been discovered that nonlinearity in photochemical systems, like in other nonlinear systems (e.g., refs. 1 and 2), can lead to intricate dynamical phenomena (3, 4) such as multiple steady states, limit cycle oscillations, and even chaos, in the context of Earth's atmosphere (5–22). For example, with a simplified box model for tropospheric photochemistry, Field et al. (18) found a threshold of NO emission flux below which the chemical system evolves toward a unique steady state and above which the system evolves toward a self-sustained oscillatory state. In this paper, we present a self-sustained oscillatory solution for an exoplanetary atmosphere, in which the abundances of ozone and other atmospheric species undergo large-magnitude periodic oscillations, despite nonvarying external forcings such as emission and stellar insolation.

The simulation is performed using a fully coupled three-dimensional (3D) atmospheric chemistry-radiation-dynamics model. We use the planetary parameters of TRAPPIST-1e, a tidally locked terrestrial exoplanet located in the middle of the habitable zone of a late M dwarf TRAPPIST-1 (23). Previous studies suggested that TRAPPIST-1e more likely hosts liquid water than all its six planetary siblings (24), so it has become a prioritized target for atmospheric characterization and the search for biosignatures with the James Webb Space Telescope (*JWST*, 25–27) and future telescopes.

As in previous studies of self-oscillations in photochemistry (9–22), we focus on ozone chemistry with ozone destruction pathways catalyzed by HO_x (defined as OH + HO_2) and NO_x (defined as NO + NO_2). Ozone (O_3) is of particular interest to the chemistry of terrestrial exoplanets and the search for extrasolar biosignatures of photosynthetic life (28, 29) because it is a photochemical product of O_2 and O_2 is a product of photosynthesis and the driver for aerobic metabolism (30, 31). While O_2 has a few absorption bands in the visible and near-infrared region, O_3 has a much stronger absorption band at 9.6 μm. Because of this, O_3 detection at 9.6 μm is a good proxy for O_2, especially for Proterozoic-like, low-O_2 atmospheres, as ozone abundance as well as its absorption and emission decreases only mildly as O_2 abundance decreases by orders of magnitude (32–34). Moreover, in cloudy atmospheres, surface-emitted, biogenic trace gases may hide beneath clouds, which mutes their spectral features. In comparison, ozone layers can be more readily observed because they are mainly located in the stratosphere, above any opaque tropospheric clouds.

Author contributions: Y.L., Y.H., and Y.L.Y. designed research; Y.L. performed research; Y.L., J.Y., and M.Z. contributed new reagents/analytic tools; Y.L., Y.H., and Y.L.Y. analyzed data; and Y.L., Y.H., and Y.L.Y. wrote the paper.

The authors declare no competing interest.

This article is a PNAS Direct Submission.

[1]To whom correspondence may be addressed. Email: yyhu@pku.edu.cn or yly@caltech.edu.

This article contains supporting information online at https://www.pnas.org/lookup/suppl/doi:10.1073/pnas.2309312120/-/DCSupplemental.

Published December 13, 2023.

Transiting exoplanets, such as TRAPPIST-1e, have a favorable feature that their atmospheres, if present, can be screened spectroscopically, so that their atmospheric compositions can be deduced from absorption features in the transmission spectrum. To facilitate the interpretation of atmospheric spectra collected in the near future, 1D (in altitude) photochemical models have been employed to study the atmospheric photochemistry of these exoplanets. Possible spectroscopic features in the transmission spectrum have been derived (e.g., refs. 35–39). The potential of detecting O_3 has been confirmed (40), but challenges are also evident given the limited signal-to-noise ratio and the lifespan of present telescopes.

Recently, simulations using fully coupled 3D chemistry-radiation-dynamics models have been performed for hypothetical atmospheres of synchronously rotating terrestrial exoplanets with Earth-like background atmospheric compositions (41–47). Ozone abundances similar to that on Earth have been produced, but the spatial distributions are different—on Earth, there is more ozone at high latitudes, whereas the simulated ozone on tidally locked exoplanets is preferentially distributed over the nightside. Because of the high computational cost of fully coupled 3D atmospheric chemistry-radiation-dynamics simulations, all these simulations have been integrated for no more than several decades, so they were unable to reveal temporal variabilities in ozone chemistry over long timescales. In this paper, we report a fully coupled 3D atmospheric chemistry-radiation-dynamics simulation that is integrated for more than seven hundred Earth years to demonstrate the possibility of multidecadal self-oscillations of ozone abundance on M-dwarf exoplanets. The reported periodic oscillations are not driven by stellar activities (45, 47, 48), seasonal cycles, or atmospheric dynamics alone (49); instead, they are self-sustained under nonvarying external forcings.

Results

Periodic Oscillations of Trace Gas Abundances. In the simulation, the atmospheric O_2 mixing ratio is set to one percent of the present atmospheric level, which is approximately the O_2 mixing ratio in the Proterozoic Eon (50). The stellar spectrum is a synthesized TRAPPIST-1 spectrum that has a moderate ultraviolet (UV) emission flux (51, see *Materials and Methods*). The emission of nitrogen oxides (NO_x) into the atmosphere mainly includes two terms—a model default surface emission flux of NO and a lightning emission flux of NO. The former totals 8 Tg (8×10^{12} g) N per Earth year, consistent with reconstructed surface NO emission rates on the pre-industrial Earth (52–54). It mostly originates from biological nitrogen fixation. The latter is parameterized (55, 56) and only totals about 0.1 Tg N per year (*SI Appendix*, Fig. S1*A*), almost negligible in the total NO_x source. Detailed information about model setup and experiment design can be found in the *Materials and Methods*.

Over more than 700 Earth years, the atmospheric abundances of ozone and nitrogen oxides undergo seven cycles, as shown in Fig. 1. The average cycle period is about 100 Earth years. The global mean O_3 abundance oscillates between 10 Dobson Units

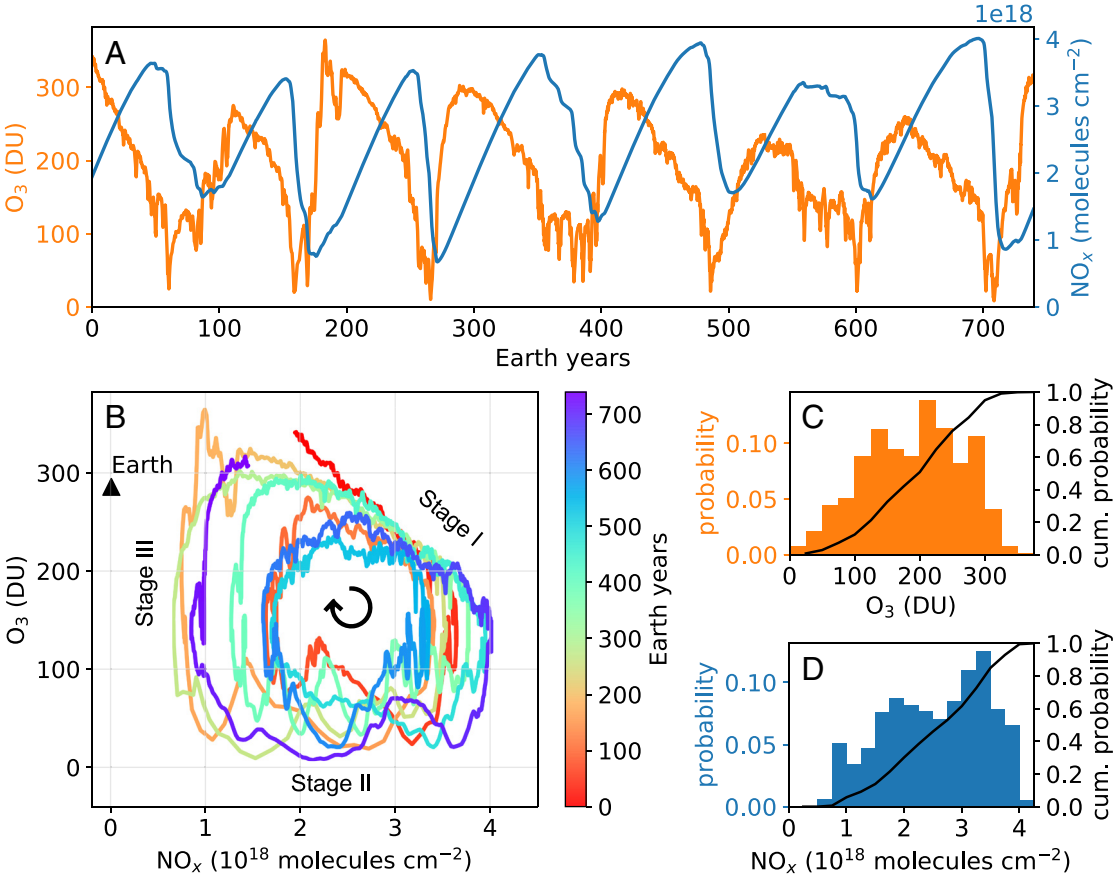

Fig. 1. Time variability of O_3 and NO_x abundances. (*A*) Time series of global mean column abundances of O_3 and NO_x. 1 DU ≈ 2.69×10^{16} molecules cm^{-2}. (*B*) Phase diagram of the system. The horizontal and vertical axes show global mean total column abundances of NO_x and O_3, respectively. The state of the photochemical system moves clockwise, as indicated by the circle arrow at the center. Colors show model time. The black triangle denotes the state of the pre-industrial Earth, where NO_x abundance is 2 to 3 orders of magnitude smaller than that in the exoplanet simulation. (*C*) and (*D*) show the PDFs (vertical bars and left axes) and CDFs (curves and right axes) of the O_3 and NO_x abundances, respectively.

(DU) and 360 DU. Meanwhile, NO_x abundance varies between 7×10^{17} molecules cm^{-2} and 4×10^{18} molecules cm^{-2}. O_3 abundance is well anticorrelated with NO_x abundance if the latter is shifted forward by 20 y. The average O_3 and NO_x abundances are 190 DU and 2.5×10^{18} molecules cm^{-2}, respectively.

Every cycle consists of three stages (Fig. 1*B*). In stage I, ozone abundance decreases as NO_x abundance increases, requiring more than half a cycle. In stage II, NO_x abundance decreases by 50 to 75%, while ozone abundance stays low and fluctuates sometimes. The duration of stage II takes about one-fifth of a cycle. In stage III, the ozone layer is restored while NO_x abundance stays low. The duration of stage III takes about one-fifth of a cycle.

Fig. 1 *C* and *D* show the probability distribution functions (PDFs) and the cumulative distribution functions (CDFs) of O_3 and NO_x abundances over the simulation. The 10th and the 90th percentiles of ozone abundance are 90 DU and 290 DU, respectively. For NO_x, they are 1.3×10^{18} molecules cm^{-2} and 3.6×10^{18} molecules cm^{-2}, respectively. These temporal variabilities could leave a signature in the transmission spectrum of the exoplanetary atmosphere, as discussed in the Observational Prospects section.

Mechanisms Behind the Self-Oscillations. The oscillations in Fig. 1 are driven by a negative feedback loop which comprises interactions between photochemistry, radiative transfer, and atmospheric dynamics in the stratosphere. Fig. 2 illustrates the key mechanisms from a simplified time-altitude perspective.

In stage I, an ozone layer exists in the middle stratosphere as a result of O_2 photolysis (Fig. 3*A*). Ozone absorbs stellar UV radiation, which warms local air and causes strong thermal inversion at the base of the ozone layer. The strong inversion is characterized by a high buoyancy frequency (N), as shown in Fig. 3*B*. Vertical motion is suppressed in this strongly stratified layer, so the vertical exchange of air between the ozone layer above it and the atmosphere below it is inefficient.

In the meantime, NO_x is emitted into the atmosphere from the surface. On Earth, tropospheric NO_x can be quickly destroyed by the reaction

$$NO_2 + OH + M \rightarrow HNO_3 + M, \quad [1]$$

where M denotes any air molecule, and the replenishment of OH relies on the photolysis of tropospheric O_3 by UV to produce $O(^1D)$, followed by $O(^1D) + H_2O \rightarrow 2OH$. On the simulated exoplanet (orbiting a cool M dwarf star), however, UV insolation is weak, so tropospheric OH concentration is low and NO_x removal is sluggish. As a result, NO_x steadily accumulates in the troposphere and in the lower stratosphere, below the aforementioned strongly stratified layer (Fig. 3*C*). This accumulation of NO_x is similar to the findings in refs. 6 and 7.

In the strongly stratified layer, a small amount of O_3 diffused from above is in contact with a small amount of NO_x diffused from below and is thus consumed, as NO_x is a catalyst for ozone removal through the following reactions

$$NO + O_3 \rightarrow NO_2 + O_2, \quad [2]$$

$$NO_2 + O \rightarrow NO + O_2, \quad [3]$$

$$O_3 + h\nu \rightarrow O + O_2, \quad [4]$$

The net reaction is

$$2O_3 \rightarrow 3O_2. \quad [5]$$

Thus, the ozone layer is slowly undermined from below, causing its base to retreat upwards. In the meantime, NO_x also slowly migrates upward through the strongly stratified layer and weakens the bulk ozone layer in the upper stratosphere through the same reactions.

As the base of the ozone layer retreats upward, the strongly stratified layer moves upward concomitantly, allowing NO_x to occupy higher altitudes (Fig. 3*C*). Thus, O_3 keeps in contact with

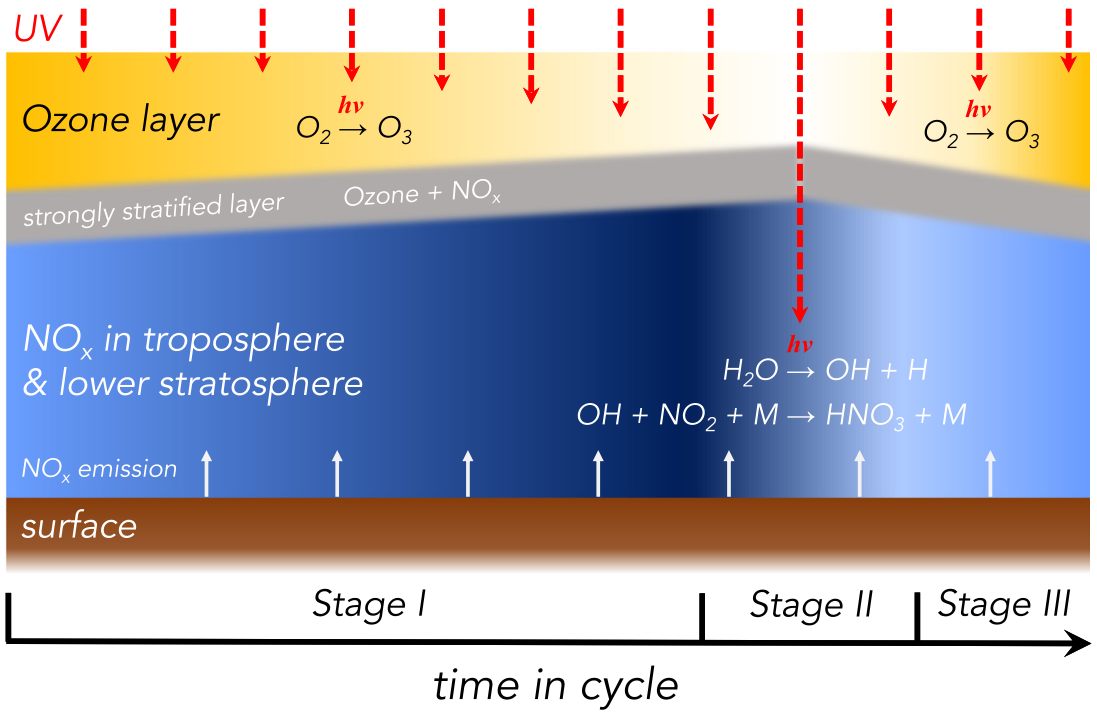

Fig. 2. A schematic diagram showing key processes in the negative feedback loop that drive the self-oscillations from a simplified time-altitude perspective. Change in the yellow (blue) color denotes change in the concentration of ozone (NO_x).

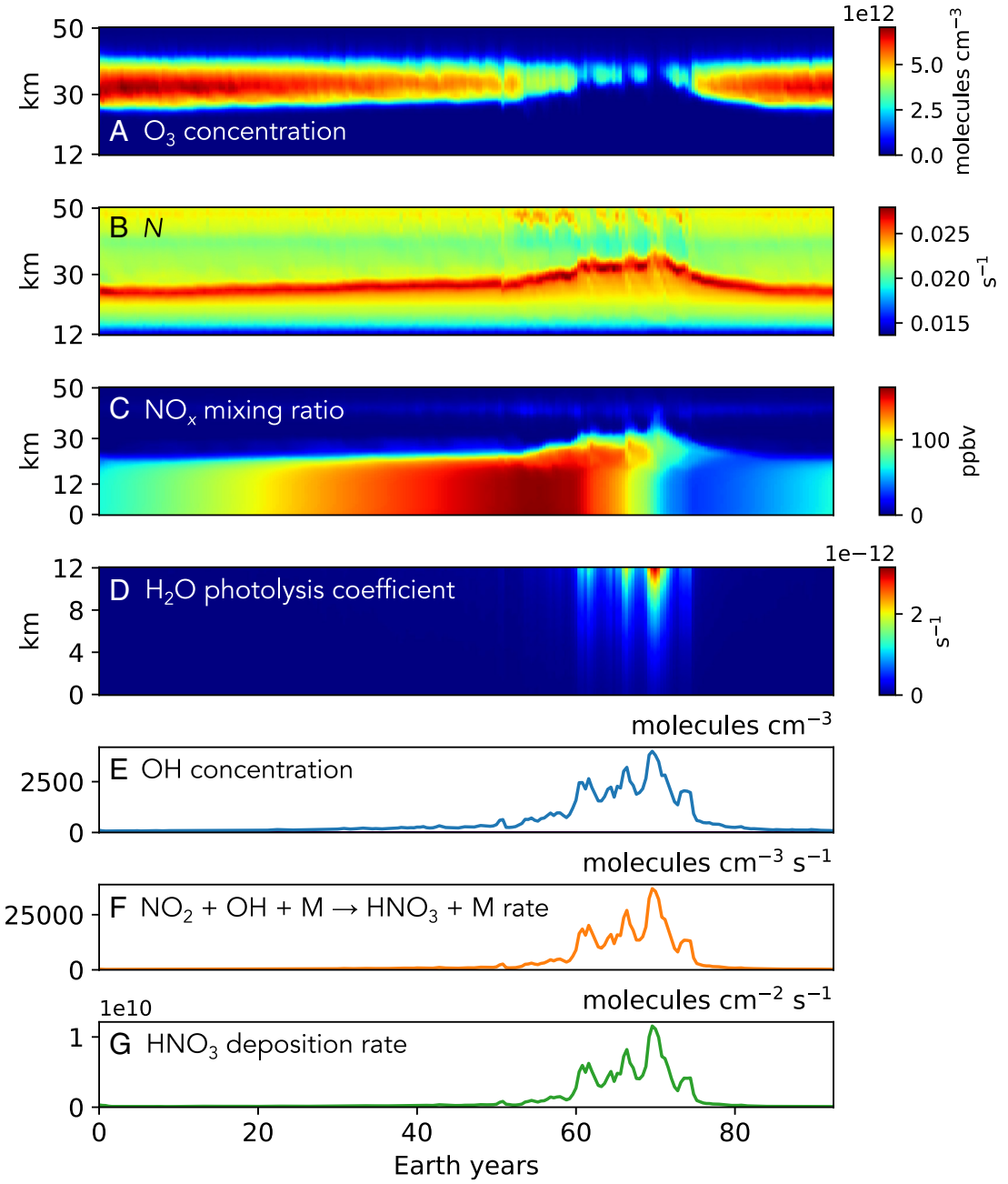

Fig. 3. Evolution of the self-oscillatory system within a cycle. Panels show time-dependent horizontal mean (*A*) ozone number density, (*B*) buoyancy frequency *N*, (*C*) NO_x mixing ratio in units of parts-per-billion-by-volume (ppbv), (*D*) the reaction rate coefficient for water vapor photolysis, (*E*) OH number density at 500 m altitude, (*F*) reaction rate of NO_2 + OH + M → HNO_3 + M at 500 m altitude, and (*G*) wet deposition rate of HNO_3. The horizontal axis is time in Earth years. The vertical axis in panels (*A*, *B*, *C*, and *D*) is altitude in kilometers. Data are taken from the fourth cycle.

NO_x in the strongly stratified layer, and the base of the ozone layer continues to be destroyed. Eventually, when NO_x abundance reaches its maximum, ninety percent of the ozone is removed (Fig. 3*A*). The duration of stage I can be approximated by dividing the increase of NO_x abundance during stage I by the surface emission flux of NO_x. A larger surface emission flux of NO can result in a shorter duration of stage I. Sensitivity tests show that tripling the surface NO flux could shorten the duration of stage I from 75 y to only 40 y (*SI Appendix*, Fig. S2).

It is a regime change in the stratospheric circulation pattern that causes the sudden decrease in the ozone abundance at the end of stage I (Fig. 4). The stratospheric circulation pattern, in turn, is determined by the distribution of ozone, the main absorbing molecules. In early to middle stage I, stratospheric NO_x concentration is low, so the lifetime of ozone is so long that ozone can be transported by tropical westerlies from the substellar region (where it is produced) to the nightside and ultimately back to the dayside, forming a tropical ozone belt (Fig. 4*A*). The heating by ozone results in an almost longitudinally symmetric pattern of atmospheric pressure (Fig. 4*C*, note that at the same altitude, atmospheric pressure is higher where the geopotential height of an isobaric surface is higher), resulting in two polar cyclones. At the same altitude, NO_x concentration is highest in the high latitudes (mostly in the northern high latitudes due to asymmetry in the land distribution over the two hemispheres) (Fig. 4*E*). NO_x is distributed far from the ascending air in the substellar region, making the upward migration of NO_x difficult.

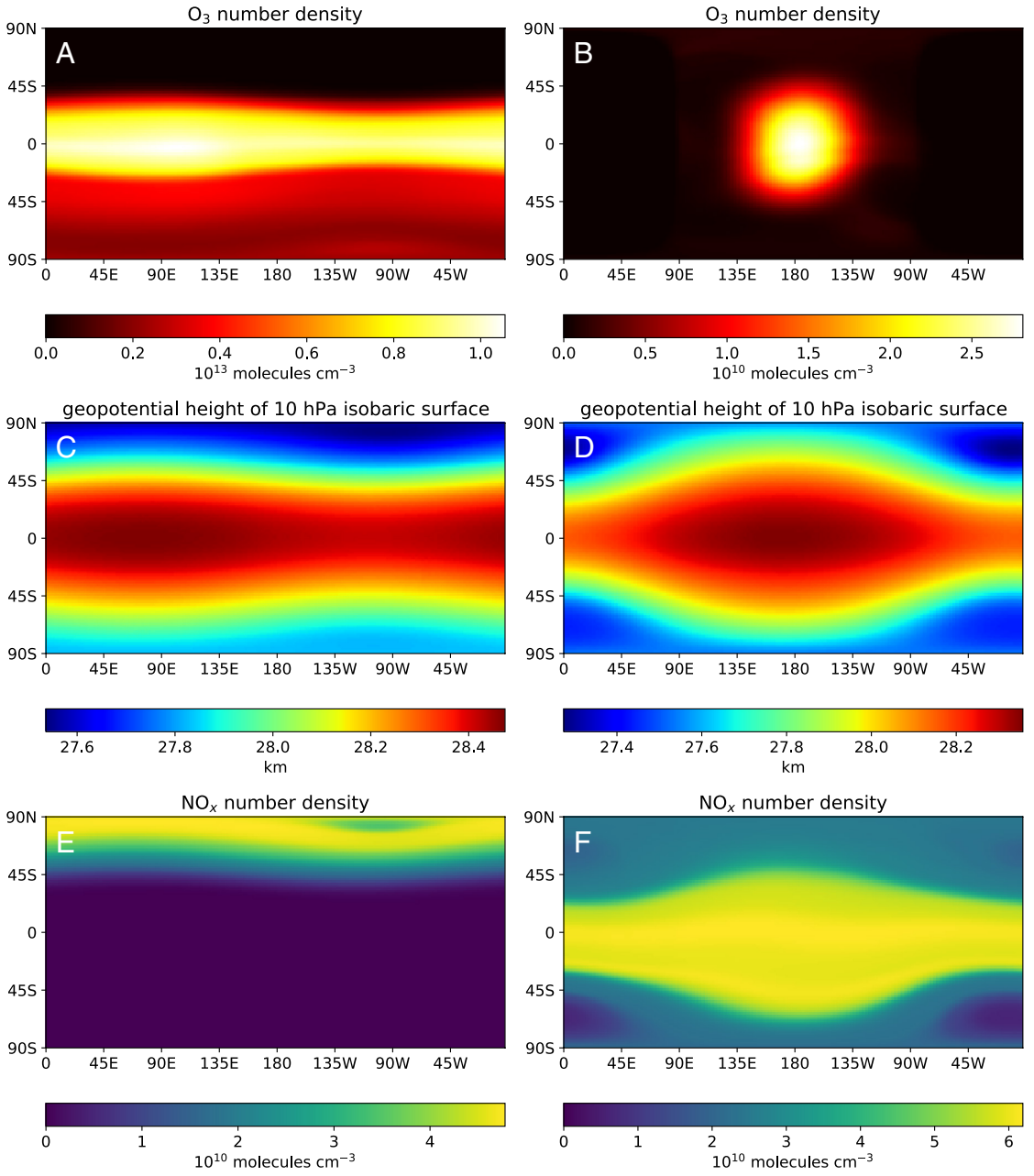

Fig. 4. Atmospheric dynamics in the stratosphere greatly affects ozone abundance. Panels (*A* and *B*) show the horizontal distribution of ozone number density in the middle stratosphere (10 hPa). Note that they have different color bars. Panels (*C* and *D*) show the horizontal distribution of the geopotential height of the 10 hPa isobaric surface. Wind is directed along the isolines. Panels (*E* and *F*) show the horizontal distribution of NO_x number density in the middle stratosphere (10 hPa). Panels (*A*, *C*, and *E*) show snapshots in early stage I (when the stratospheric ozone layer is thick). Panels (*B*, *D*, and *F*) show snapshots near the end of stage I, when the stratospheric ozone layer has been greatly attenuated. The substellar point is located at the center of each panel.

However, close to the end of stage I, NO_x concentration in the middle stratosphere is high enough to reduce the lifetime of ozone below the timescale it takes to transport ozone out of the substellar region. As a result, ozone is confined around the substellar point (Fig. 4*B*), which then results in localized heating in the substellar region. Isobaric surfaces in the substellar region are thus lifted, forming a spindle-shaped distribution of atmospheric pressure (Fig. 4*D*). The abrupt change in the circulation pattern drives NO_x from the high-latitude barometric lows to the low-latitude barometric highs, also forming a spindle-shaped distribution of NO_x concentration (Fig. 4*F*). The high NO_x concentration in the substellar region then makes the upward NO_x transport by substellar ascending air very efficient. Large amounts of NO_x rapidly rise to the upper stratosphere where the ozone layer is located and destroy the remaining ozone, causing a sudden decrease in ozone abundance (Fig. 1*B*), marking the end of stage I. Such a regime change in stratospheric circulation occurs multiple times during stage II and causes the fast oscillations in ozone abundances in stage II (Fig. 1 *A* and *B*).

In stage II, depleted stratospheric ozone allows UV radiation to reach the lower troposphere, leading to rapid photolysis of water vapor and a rapid increase in OH concentration (Fig. 3 *D* and *E*). Note that this mechanism holds only when the atmospheric O_2 level is low, as high O_2 levels would not allow UV to reach the lower troposphere. Then, abundant OH leads to a rapid decline of NO_x through Reaction 1 (Fig. 3*F*), during which more than

half of the NO_x is removed. The product of this reaction, nitric acid (HNO_3), is then scavenged out of the atmosphere by wet deposition (Fig. 3*G*), which balances NO emission and closes the atmospheric budget of NO_y (defined as NO + NO_2 + NO_3 + HNO_3 + HO_2NO_2 + 2 N_2O_5 + $ClONO_2$ + $BrONO_2$). In stage III, the NO_x abundance is at its minimum (Fig. 3*C*), so the catalytic cycle for ozone loss is slow, allowing the stratospheric ozone layer to be restored (Fig. 3*A*). The system then enters the next cycle.

Observational Prospects. Both the ozone layer and its variability can be detected by transit spectroscopy (Fig. 5). Averaged over the seven cycles and assuming a resolving power $\lambda/\Delta\lambda$ = 100, starlight absorption by ozone enhances the transit depth at 9.6 μm by 60 parts-per-million (ppm, Fig. 5 *A* and *C*). Detection of this signal will be challenging for *JWST* (40) but is possible for future instruments dedicated for atmospheric characterization of transiting exoplanets. Fig. 5 *B* and *D* show the temporal variability of the transit depths. The largest variability takes place at the wings of the 9.6-μm ozone absorption band. At 9.82 μm, the variability is up to 50 ppm. The variability is smaller at the center of the ozone absorption band due to line saturation.

The PDF and the CDF of the transit depth at 9.82 μm are shown in Fig. 5*E*. Despite the symmetry in the PDF of the ozone abundance in Fig. 1*C*, the distribution of the transit depth is left-skewed because of line saturation at high ozone abundance. The 10th and the 90th percentiles are 25 ppm and 47 ppm respectively. The variability of NO_x absorption features is hardly detectable. A clear-sky condition is assumed in the transit depth calculations presented above. Refer to *SI Appendix*, Figs. S3 and S4 for the effect of cloud on the transit depth calculations.

Discussion

Our results show that large-magnitude self-sustained oscillations in atmospheric chemistry can exist on exoplanets, which may induce significant temporal variability in transmission spectra of exoplanetary atmospheres. Such variability could be detected by future observations that revisit atmospheric spectra of exoplanets over long periods of time. Although a complete cycle may be too long to observe, steady trends in ozone abundance, such as the decreasing trend in stage I and the increasing trend in stage III, if observed, could also suggest the possible presence of such oscillations.

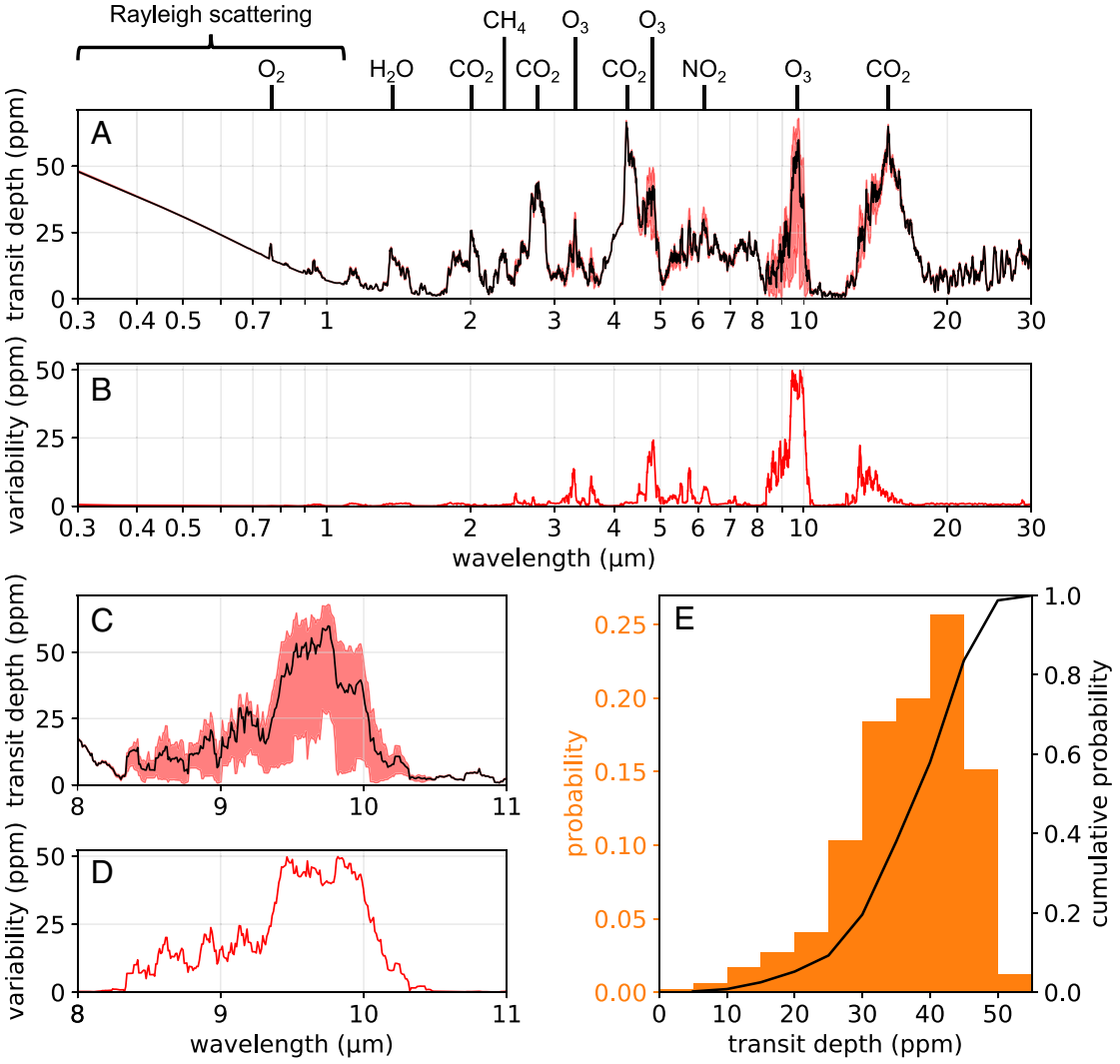

Fig. 5. Detectability of the ozone layer and its variability. (*A*) Wavelength-dependent transit depth of the atmosphere. The black curve shows the time mean transit depth. The red shading shows the range of transit depths over the entire simulation. A moving average with a resolving power of 100 (the resolving power of *JWST*'s low-resolution spectroscopy) is applied. (*B*) Variability in the transit depth (maximum minus minimum) over the seven cycles. (*C*) and (*D*) are the same as (*A*) and (*B*), but in the vicinity of the 9.6 μm ozone absorption band. (*E*) The PDF (vertical bars and left axis) and CDF (curve and right axis) of the transit depth at 9.82 μm.

Sensitivity tests show that without the surface NO_x emission, which mainly originates from biological nitrogen fixation, the large-magnitude self-oscillations would not occur (*SI Appendix*, Fig. S2). This is consistent with previous findings that tropospheric photochemical systems produce self-oscillations only if the NO emission flux exceeds a certain threshold (18). Therefore, we proposed that the large-magnitude, slow, and periodic temporal variability in ozone abundance reported in this paper is a biosignature because they could suggest the presence of a strong NO_x source that is probably biological. This unique class of biosignature is intrinsically different from the conventional ideas of oscillations of atmospheric gases being biosignatures (31) which arise from the nonuniform spatial distribution of a biosphere and the seasonality in insolation conditions. By contrast, the self-oscillations in this paper do not rely on either of the two conditions, and their period can be completely unrelated to the orbital period. The variabilities reported in this paper can also be distinguished from those induced by atmospheric dynamics (49) and those induced by cloud dynamics (57), as the latter two usually happen on shorter timescales and have smaller magnitudes.

It is worth noting that the UV spectrum of the host star, the oxygen level in the planetary atmosphere, the water vapor supply, the NO_x emission rate, and other physical parameters, could all potentially affect the oscillation properties such as magnitude and period, or determine whether self-oscillations can exist at all. Because of the computational cost of fully coupled, 3D atmospheric chemistry-radiation-dynamics simulations, a systematic investigation for the dependence on these multiple parameters will be left for future work.

Oscillations in photochemical systems akin to those in this paper could have induced the observed variabilities on solar-system planets (58) and exoplanets (59–62), although the nature of the oscillations can be completely different in different planetary contexts.

It is intriguing to ponder whether similar photochemical oscillations occurred in Earth's history, and if they did, what discernible traces might be preserved in geological records. Some processes within the oscillations may have occurred on paleo-Earth, such as the destruction of the ozone layer by substantial NO_x production during large impact events, followed by the conversion of NO_x to HNO_3 and the rainout of HNO_3 that acidified the ocean. This hypothesis finds support in the selective extinction of calcareous-shelled organisms that inhabited the shallow marine environments at the end of the Cretaceous period (63).

Materials and Methods

Fully Coupled 3D Atmospheric Chemistry-Radiation-Dynamics Simulations. The fully coupled, 3D atmospheric chemistry-radiation-dynamics model used here is Community Earth System Model-Whole Atmosphere Community Climate Model (CESM-WACCM) (64). CESM (version 1.2.2) is a fully coupled, community, global climate model that includes interactions of atmosphere, land, ocean, sea ice, etc. WACCM (version 4.0) serves as its atmosphere component. WACCM has fully coupled, 3D atmospheric dynamics, photochemistry, and radiative transfer and has been extensively used to simulate ozone chemistry in the Earth's atmosphere (65). With the top layer reaching about 6×10^{-4} Pa, WACCM fully resolves the stratosphere. The photochemistry component of WACCM is the Model for Ozone and Related Chemical Tracers chemical transport model (version 4) (66). It has 57 atmospheric species including neutral and ion constituents, and one inert atmospheric species (N_2). These species are linked by 74 photolytic and ionization reactions, 143 gas phase reactions, and 17 heterogeneous reactions on aerosol particles. The model resolves the full ozone chemistry by simulating all major reactions involving O_x (defined as $O_x = O_3 + O$), HO_x, NO_x, ClO_x (defined as Cl + ClO), and BrO_x (defined as Br + BrO). Nitrogen chemistry involving all NO_y species is also resolved.

We assume a preindustrial chemical scenario in which only HO_x and NO_x are important catalysts for ozone loss. For boundary conditions, the model prescribes volume mixing ratios of O, O_2, H, H_2, N, NO, CO, and CO_2 at the upper boundary (model top) and volume mixing ratios of H_2, CH_4, CH_3Cl, CH_3Br, N_2O, and CO_2 at the lower boundary (surface). Emission in the model includes surface fluxes of NO, HCHO, and CO and a lightning flux of NO. The model default surface emission flux of NO is 8 Tg N per year. The simulated lightning emission of NO is about two orders of magnitude smaller than that on Earth due to the low O_2 level and tidal locking, the latter confining lightning flashes within the substellar region. For deposition, there are dry depositions of O_3, H_2O_2, NO_2, HNO_3, HO_2NO_2, CH_3OOH, HCHO, and CO and wet depositions of H_2O_2, HNO_3, HO_2NO_2, HCl, HOCl, $ClONO_2$, HOBr, HBr, $BrONO_2$, CH_3OOH, and HCHO.

For other components of CESM, the land component used here is the diagnostic version of the Community Land Model (CLM), and the ocean component has fixed sea surface temperature and fixed sea ice distribution. The sea surface temperature and sea ice distribution are taken from one simulation for TRAPPIST-1e with 400 parts-per-million-by-volume (ppmv) CO_2 (24) (*SI Appendix*, Fig. S5). Sea ice temperature is calculated. The Earth's land–sea distribution and topography are used in the simulation.

The substellar point is fixed at 0°N, 180°E. The rotation period is set to 6.1 Earth days. The orbital eccentricity and obliquity are set to zero. The background atmosphere is composed of 99.79% N_2 and 0.21% O_2. To account for the effect of the low O_2 concentration, we scaled the NO emission flux from lightning by a factor of 0.103, a value obtained from thermodynamic equilibrium. The mean molecular weight of dry air is set to 28.128 g mol^{-1}. For simplicity, we use Earth's radius and surface gravity to approximate those of TRAPPIST-1e. The quasi-biennial oscillation

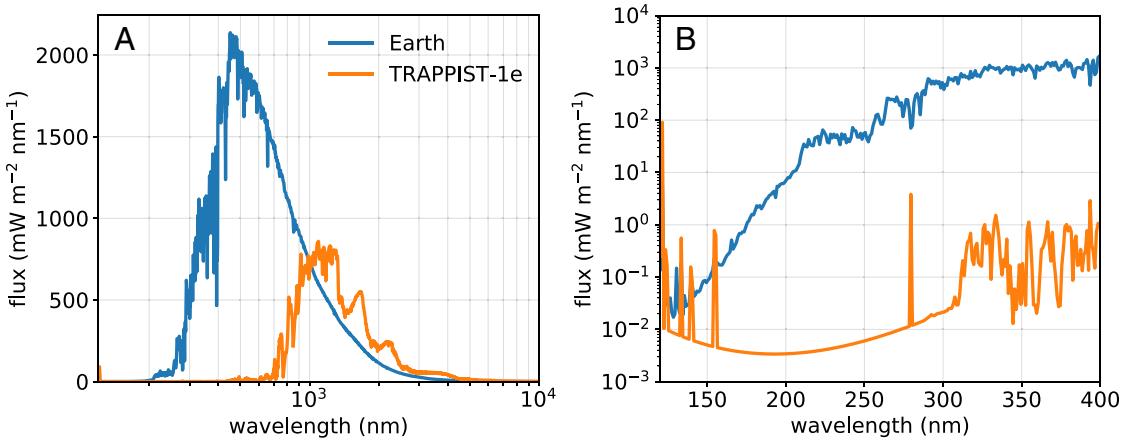

Fig. 6. The M-dwarf stellar spectrum used in the simulation, in comparison to the solar spectrum. (*A*) Panchromatic and (*B*) UV spectra of the incoming stellar radiation at the top of the atmospheres of Earth (blue curve) and TRAPPIST-1e (orange curve). The emission lines in (*B*) include H I (Lyα), N V, C II, Si IV, C IV, Mg II, and Ca II lines (51).

forcing in WACCM, which is a momentum forcing in the tropical stratosphere, is turned off. CO_2 concentration is set to 400 ppmv. The seasonality in all boundary conditions, including those on volume mixing ratios and those on emission fluxes, is smoothed out.

Stellar Spectrum. The stellar spectrum used here is from the Mega-MUSCLES Treasury Survey (51 Fig. 6). It was produced by synthesizing observations from the NASA Hubble Space Telescope (*HST*) and XMM-Newton and simulations using stellar models for the photosphere, chromosphere, transition region, and corona. The wavelength ranges of particular importance to photochemistry, i.e., far-UV (120 to 170 nm) and near-UV (170 to 320 nm), are primarily determined from measurements by the Cosmic Origins Spectrograph on board HST, with data gaps between 210 nm and 280 nm filled by interpolation. The spectrum is scaled to reproduce the total incident radiative energy flux at TRAPPIST-1e–879.2 W m^{-2}. In far-UV, the simulated exoplanet receives seven times more radiative energy than Earth, whereas in near-UV, it receives only 0.03% of the radiative energy received by Earth.

Calculation of the Transmission Spectra. The transmission spectra are calculated using Exo-Transmit (67). Users need to specify planetary and stellar radii, a planet's surface gravity, a temperature-pressure profile of the atmosphere, and concentration-pressure profiles for a variety of atmospheric species. In the transmission spectrum calculation, we set the planetary radius to 5,798 km, the radius of TRAPPIST-1e, and set the stellar radius to 82,930 km, the radius of TRAPPIST-1. The surface gravity of the planet is set to 9.8 m s^{-2}. We include 16 species–CH_4, CO, CO_2, H, HCl, H_2, H_2CO, H_2O, N, N_2, NO_2, NO, O, O_2, O_3, and OH. Exo-Transmit then finds atmospheric opacity by interpolating between single-molecule cross-section data for CH_4, CO, CO_2, HCl, H_2CO, H_2O, N_2, NO_2, NO, O_2, O_3, and OH between a predefined temperature-pressure grid (temperature ranging from 100 K to 3,000 K with a spacing of 100 K, pressure ranging from 10^{-4} Pa to 10^8 Pa with a spacing of one order of magnitude) and collision-induced-absorption opacity data for CH_4–CH_4, CO_2–CO_2, H_2–H_2, H_2–H, H_2–CH_4, N_2–CH_4, N_2–H_2, N_2–N_2, O_2–CO_2, O_2–N_2, and O_2–O between the same temperature grid, solves the radiative transfer equation using opacity sampling at a resolving power of 1,000, and generates wavelength-dependent transit depths. The wavelength range is between 300 nm and 30 μm. Exo-Transmit considers the oblique path of light through the planetary atmosphere along a distant observer's line of sight. It also accounts for opacity caused by Rayleigh scattering. All opacity data in Exo-Transmit are taken from refs. 68–70.

We carry out Exo-Transmit calculations for 10^{-3} to 10^5 Pa of the modeled atmosphere. To account for 3D effects, we calculate a spectrum for every latitude on the terminator of the planet and average all output transmission spectra. To account for potential cloud effects that mute molecular absorption features, we also carry out calculations with an optically thick cloud deck at 100 hPa (*SI Appendix*, Figs. S3 and S4). One can find the lower bound of the transit depths in these cloudy scenarios.

Data, Materials, and Software Availability. Data generated from WACCM and Exo-Transmit that is used for the analysis in this study is uploaded to the CaltechDATA repository: https://doi.org/10.22002/7yh5j-c4865 (71). The stellar spectrum used in this study can be accessed at ref. 72. All other data are included in the manuscript and/or *SI Appendix*.

ACKNOWLEDGMENTS. We thank Stuart Bartlett for composing the title of the paper, helpful discussions, and critical reading of the paper and Danica Adams for helpful discussions and critical reading of the paper. This work is supported by National Natural Science Foundation of China grant 41888101 (Y.H. and J.Y.), California Institute of Technology grant YLY.2500006-1-OAID.CITRESRCH (Y.L.), and Virtual Planetary Laboratory, the University of Washington (Y.L.Y.). Portions of the paper were developed from Y.L.'s thesis.

Author affiliations: [a]Division of Geological and Planetary Sciences, California Institute of Technology, Pasadena, CA 91125; [b]Department of Atmospheric and Oceanic Sciences, School of Physics, Peking University, Beijing 100871, China; and [c]Laboratoire de Météorologie Dynamique/Institut Pierre-Simon Laplace, Sorbonne Université, École Normale Supérieure, Université Paris Sciences et Lettres, Ecole Polytechnique, Institut Polytechnique de Paris, Centre National de la Recherche Scientifique, Paris 75005, France

1. L. Sertorio, G. Tinetti, Prey-predator dynamics driven by the solar radiation. Part I. *Nuovo Cimento C* **23**, 635–654 (2000).
2. L. Sertorio, G. Tinetti, Prey-predator dynamics with periodic solar input. Part II. *Nuovo Cimento C* **23**, 655–678 (2000).
3. S. H. Strogatz, *Nonlinear Dynamics and Chaos: With Applications to Physics, Biology, Chemistry, and Engineering* (Perseus Books Publishing, L.L.C., 1994).
4. A. J. Lichtenberg, M. A. Lieberman, *Regular and Chaotic Dynamics* (Springer Science+Business, Media, L.L.C., 2013).
5. M. J. Prather, M. B. McElroy, S. C. Wofsy, J. A. Logan, Stratospheric chemistry: Multiple solutions. *Geophys. Res. Lett.* **6**, 163–164 (1979).
6. W. H. White, D. Dietz, Does the photochemistry of the troposphere admit more than one steady state? *Nature* **309**, 242–244 (1984).
7. J. F. Kasting, T. P. Ackerman, High atmospheric NO_x levels and multiple photochemical steady states. *J. Atmos. Chem.* **3**, 321–340 (1985).
8. R. W. Stewart, Multiple steady states in atmospheric chemistry. *J. Geophys. Res. Atmos.* **98**, 20601–20611 (1993).
9. R. W. Stewart, Dynamics of the low to high NO_x transition in a simplified tropospheric photochemical model. *J. Geophys. Res. Atmos.* **100**, 8929–8943 (1995).
10. M. C. Krol, Comment on "Multiple steady states in atmospheric chemistry" by Richard W. Stewart. *J. Geophys. Res. Atmos.* **100**, 11699–11702 (1995).
11. A. M. Feigin, I. B. Konovalov, On the possibility of complicated dynamic behavior of atmospheric photochemical systems: Instability of the Antarctic photochemistry during the ozone hole formation. *J. Geophys. Res. Atmos.* **101**, 26023–26038 (1996).
12. D. Poppe, H. Lustfeld, Nonlinearities in the gas phase chemistry of the troposphere: Oscillating concentrations in a simplified mechanism. *J. Geophys. Res. Atmos.* **101**, 14373–14380 (1996).
13. P. G. Hess, S. Madronich, On tropospheric chemical oscillations. *J. Geophys. Res. Atmos.* **102**, 15949–15965 (1997).
14. M. C. Krol, D. Poppe, Nonlinear dynamics in atmospheric chemistry rate equations. *J. Atmos. Chem.* **29**, 1–16 (1998).
15. A. M. Feigin, L. B. Konovalov, Y. I. Molkov, Toward an understanding of the nonlinear nature of atmospheric photochemistry: Essential dynamic model of the mesospheric photochemical system. *J. Geophys. Res. Atmos.* **103**, 25447–25460 (1998).
16. I. B. Konovalov, A. M. Feigin, A. Y. Mukhina, Toward understanding of the nonlinear nature of atmospheric photochemistry: Multiple equilibrium states in the high-latitude lower stratospheric photochemical system. *J. Geophys. Res. Atmos.* **104**, 3669–3689 (1999).
17. I. B. Konovalov, A. M. Feigin, Toward an understanding of the nonlinear nature of atmospheric photochemistry: Origin of the complicated dynamic behaviour of the mesospheric photochemical system. *Nonlin. Processes Geophys.* **7**, 87–104 (2000).
18. R. J. Field, P. G. Hess, L. V. Kalachev, S. Madronich, Characterization of oscillation and a period-doubling transition to chaos reflecting dynamic instability in a simplified model of tropospheric chemistry. *J. Geophys. Res. Atmos.* **106**, 7553–7565 (2001).
19. L. V. Kalachev, R. J. Field, Reduction of a model describing ozone oscillations in the troposphere: Example of an algorithmic approach to model reduction in atmospheric chemistry. *J. Atmos. Chem.* **39**, 65–93 (2001).
20. M. R. Tinsley, R. J. Field, Steady state instability and oscillation in simplified models of tropospheric chemistry. *J. Phys. Chem. A* **105**, 11212–11219 (2001).
21. M. R. Tinsley, R. J. Field, Dynamic instability in tropospheric photochemistry: An excitability threshold. *Geophys. Res. Lett.* **28**, 4437–4440 (2001).
22. A. S. Hasson, R. E. Manor, Steady-state instability in tropospheric chemical mechanisms. *Atmos. Environ.* **37**, 4735–4745 (2003).
23. M. Gillon *et al.*, Seven temperate terrestrial planets around the nearby ultracool dwarf star TRAPPIST-1. *Nature* **542**, 456–460 (2017).
24. E. T. Wolf, Assessing the habitability of the TRAPPIST-1 system using a 3D climate model. *Astrophys. J. Lett.* **839**, L1 (2017).
25. J. K. Barstow, P. G. Irwin, Habitable worlds with *JWST*: Transit spectroscopy of the TRAPPIST-1 system? *Mon. Not. R. Astron. Soc. Lett.* **461**, L92–L96 (2016).
26. C. V. Morley, L. Kreidberg, Z. Rustamkulov, T. Robinson, J. J. Fortney, Observing the atmospheres of known temperate Earth-sized planets with *JWST*. *Astrophys. J.* **850**, 121 (2017).
27. N. E. Batalha, N. K. Lewis, M. R. Line, J. Valenti, K. Stevenson, Strategies for constraining the atmospheres of temperate terrestrial planets with *JWST*. *Astrophys. J. Lett.* **856**, L34 (2018).
28. A. Segura *et al.*, Ozone concentrations and ultraviolet fluxes on Earth-like planets around other stars. *Astrobiology* **3**, 689–708 (2003).
29. A. Segura *et al.*, Biosignatures from Earth-like planets around M dwarfs. *Astrobiology* **5**, 706–725 (2005).
30. V. S. Meadows, Reflections on O_2 as a biosignature in exoplanetary atmospheres. *Astrobiology* **17**, 1022–1052 (2017).
31. E. W. Schwieterman *et al.*, Exoplanet biosignatures: A review of remotely detectable signs of life. *Astrobiology* **18**, 663–708 (2018).
32. A. Léger, M. Pirre, F. J. Marceau, Search for primitive life on a distant planet: Relevance of O_2 and O_3 detections. *Astron. Astrophys.* **277**, 309 (1993).
33. D. Pollard, J. F. Kasting, Snowball Earth: A thin-ice solution with flowing sea glaciers. *J. Geophys. Res. Oceans* **110**, C07010 (2005).
34. G. J. Cooke, D. R. Marsh, C. Walsh, B. Black, J. F. Lamarque, A revised lower estimate of ozone columns during Earth's oxygenated history. *R. Soc. Open Sci.* **9**, 211165 (2022).
35. J. T. O'Malley-James, L. Kaltenegger, UV surface habitability of the TRAPPIST-1 system. *Mon. Not. R. Astron. Soc. Lett.* **469**, L26–L30 (2017).
36. J. Krissansen-Totton, R. Garland, P. Irwin, D. C. Catling, Detectability of biosignatures in anoxic atmospheres with the James Webb Space Telescope: A TRAPPIST-1e case study. *Astron. J.* **156**, 114 (2018).
37. A. P. Lincowski *et al.*, Evolved climates and observational discriminants for the TRAPPIST-1 planetary system. *Astrophys. J.* **867**, 76 (2018).
38. T. J. Fauchez *et al.*, Impact of clouds and hazes on the simulated *JWST* transmission spectra of habitable zone planets in the TRAPPIST-1 system. *Astrophys. J.* **887**, 194 (2019).

39. F. Wunderlich *et al.*, Detectability of atmospheric features of Earth-like planets in the habitable zone around M dwarfs. *Astron. Astrophys.* **624**, A49 (2019).
40. J. Lustig-Yaeger, V. S. Meadows, A. P. Lincowski, The detectability and characterization of the TRAPPIST-1 exoplanet atmospheres with *JWST*. *Astron. J.* **158**, 27 (2019).
41. E. Proedrou, K. Hocke, Characterising the three-dimensional ozone distribution of a tidally locked Earth-like planet. *Earth, Planets Space* **68**, 1–20 (2016).
42. H. Chen, E. T. Wolf, R. Kopparapu, S. Domagal-Goldman, D. E. Horton, Biosignature anisotropy modeled on temperate tidally locked M-dwarf planets. *Astrophys. J. Lett.* **868**, L6 (2018).
43. H. Chen, E. T. Wolf, Z. Zhan, D. E. Horton, Habitability and spectroscopic observability of warm M-dwarf exoplanets evaluated with a 3D chemistry-climate model. *Astrophys. J.* **886**, 16 (2019).
44. J. S. Yates *et al.*, Ozone chemistry on tidally locked M dwarf planets. *Mon. Not. R. Astron. Soc.* **492**, 1691–1705 (2020).
45. H. Chen *et al.*, Persistence of flare-driven atmospheric chemistry on rocky habitable zone worlds. *Nat. Astron.* **5**, 298–310 (2021).
46. M. Braam *et al.*, Lightning-induced chemistry on tidally-locked Earth-like exoplanets. *Mon. Not. R. Astron. Soc.* **517**, 2383–2402 (2022).
47. R. J. Ridgway *et al.*, 3D modelling of the impact of stellar activity on tidally locked terrestrial exoplanets: Atmospheric composition and habitability. *Mon. Not. R. Astron. Soc.* **518**, 2472–2496 (2023).
48. A. Segura, L. M. Walkowicz, V. Meadows, J. Kasting, S. Hawley, The effect of a strong stellar flare on the atmospheric chemistry of an Earth-like planet orbiting an M dwarf. *Astrobiology* **10**, 751–771 (2010).
49. M. Cohen *et al.*, Longitudinally asymmetric stratospheric oscillation on a tidally locked exoplanet. *Astrophys. J.* **930**, 152 (2022).
50. T. W. Lyons, C. T. Reinhard, N. J. Planavsky, The rise of oxygen in Earth's early ocean and atmosphere. *Nature* **506**, 307–315 (2014).
51. D. J. Wilson *et al.*, The Mega-MUSCLES spectral energy distribution of TRAPPIST-1. *Astrophys. J.* **911**, 18 (2021).
52. J. J. Yienger, H. Levy, Empirical model of global soil-biogenic NO_x emissions. *J. Geophys. Res. Atmos.* **100**, 11447–11464 (1995).
53. A. F. Bouwman, L. J. M. Boumans, N. H. Batjes, Emissions of N_2O and NO from fertilized fields: Summary of available measurement data. *Global Biogeochem. Cycles* **16**, 6-1–6-13 (2002).
54. J.-F. Lamarque *et al.*, Historical (1850–2000) gridded anthropogenic and biomass burning emissions of reactive gases and aerosols: Methodology and application. *Atmos. Chem. Phys.* **10**, 7017–7039 (2010).
55. C. Price, D. Rind, A simple lightning parameterization for calculating global lightning distributions. *J. Geophys. Res. Atmos.* **97**, 9919–9933 (1992).
56. C. Price, J. Penner, M. Prather, NO_x from lightning: 1. Global distribution based on lightning physics. *J. Geophys. Res. Atmos.* **102**, 5929–5941 (1997).
57. X. Song, J. Yang, Asymmetry and variability in the transmission spectra of tidally locked habitable planets. *Front. Astron. Space Sci.* **8**, 134 (2021).
58. E. Marcq, J. L. Bertaux, F. Montmessin, D. Belyaev, Variations of sulphur dioxide at the cloud top of Venus's dynamic atmosphere. *Nat. Geosci.* **6**, 25–28 (2013).
59. S. Rappaport *et al.*, Possible disintegrating short-period super-Mercury orbiting KIC 12557548. *Astrophys. J.* **752**, 1 (2012).
60. O. Barragán *et al.*, K2-141 b. A 5-M⊕ super-Earth transiting a K7 V star every 6.7 h. *Astron. Astrophys.* **612**, A95 (2018).
61. P. Tamburo, A. Mandell, D. Deming, E. Garhart, Confirming variability in the secondary eclipse depth of the super-Earth 55 Cancri e. *Astron. J.* **155**, 221 (2018).
62. E. A. Meier Valdés, B. M. Morris, R. D. Wells, N. Schanche, B. O. Demory, Weak evidence for variable occultation depth of 55 Cnc e with TESS. *Astron. Astrophys.* **663**, A95 (2022).
63. J. S. Lewis, G. H. Watkins, H. Hartman, R. G. Prinn "Chemical consequences of major impact events on Earth" in Geological Implications of Impacts of Large Asteroids and Comets on Earth, L. T. Silver, P. H. Schultz, Ed. (Geol. Soc. of Amer., Sp. Pap. 190, 1982), pp. 215–221.
64. R. B. Neale *et al.*, Description of the NCAR community atmosphere model (CAM 5.0) (NCAR Technical Note NCAR/TN-486+STR, National Center for Atmospheric Research, Boulder, CO, 2012).
65. D. R. Marsh *et al.*, Climate change from 1850 to 2005 simulated in CESM1 (WACCM). *J. Clim.* **26**, 7372–7391 (2013).
66. L. K. Emmons *et al.*, Description and evaluation of the Model for Ozone and Related chemical Tracers, version 4 (MOZART-4). *Geosci. Model Dev.* **3**, 43–67 (2010).
67. E. M. R. Kempton, R. Lupu, A. Owusu-Asare, P. Slough, B. Cale, Exo-Transmit: An open-source code for calculating transmission spectra for exoplanet atmospheres of varied composition. *Publ. Astron. Soc. Pac.* **129**, 044402 (2017).
68. R. S. Freedman, M. S. Marley, K. Lodders, Line and mean opacities for ultracool dwarfs and extrasolar planets. *Astrophys. J. Suppl. Ser.* **174**, 504 (2008).
69. R. S. Freedman *et al.*, Gaseous mean opacities for giant planet and ultracool dwarf atmospheres over a range of metallicities and temperatures. *Astrophys. J. Suppl. Ser.* **214**, 25 (2014).
70. R. E. Lupu *et al.*, The atmospheres of Earthlike planets after giant impact events. *Astrophys. J.* **784**, 27 (2014).
71. Y. Luo, Data from "Beyond steady states: Coupled atmospheric chemistry, radiation and dynamics of an exoplanet produce self-sustained oscillations". CaltechDATA. https://doi.org/10.22002/7yh5j-c4865. Deposited 29 September 2023.
72. D. J. Wilson *et al.*, Mega-MUSCLES Semi-empirical SED of TRAPPIST-1. Zenodo. https://doi.org/10.5281/zenodo.4556130. Deposited 22 February 2021.